

Chiral Kondo Lattice in Doped MoTe₂/WSe₂ Bilayers

Daniele Guerci,¹ Jie Wang,¹ Jiawei Zang,² Jennifer Cano,^{3,1} J. H. Pixley,^{4,1} and Andrew Millis^{1,2}

¹Center for Computational Quantum Physics, Flatiron Institute, New York, New York 10010, USA

²Department of Physics, Columbia University, 538 West 120th Street, New York, NY 10027

³Department of Physics and Astronomy, Stony Brook University, Stony Brook, New York 11794, USA

⁴Department of Physics and Astronomy, Center for Materials Theory, Rutgers University, Piscataway, New Jersey 08854, USA

We theoretically study the interplay between magnetism and a heavy Fermi liquid in the AB stacked transition metal dichalcogenide bilayer system MoTe₂/WSe₂ in the regime in which the *Mo* layer supports localized magnetic moments coupled by interlayer electron tunnelling to a weakly correlated band of itinerant electrons in the *W* layer. We show that the interlayer electron transfer leads to a chiral Kondo exchange, with consequences including a strong dependence of the Kondo temperature on carrier concentration, a topological hybridization gap and an anomalous Hall effect. The theoretical model exhibits two phases, a small Fermi surface magnet and a large Fermi surface heavy Fermi liquid; the transition between them is first order. A low-energy theory is developed for the transport properties of the two states. Implications of our results for present and future experiments on MoTe₂/WSe₂ bilayer heterostructures are discussed.

Introduction.— Transition metal dichalcogenide (TMD) moiré devices created by stacking two TMD monolayers have recently emerged as a highly tunable platform to realize strongly correlated states [1–17]. The unit cell size and bandwidth (and hence the relative correlation strength) can be varied over wide ranges by changing either the lattice mismatch of the component materials or their relative twist angle; external gates enable both the total carrier density per unit cell and the distribution of the carriers over the two planes to be varied over a wide range. The broken inversion symmetry and strong spin orbit coupling (SOC) of the individual layers [18, 19] lead to spin-momentum locking, implying the potential for a wide variety of topological effects.

In this paper we focus on the AB-stacked MoTe₂/WSe₂ bilayer heterostructure of recent experimental [1] and theoretical [11–16] interest. In this system the lattice mismatch between the two materials leads to a hexagonal moiré lattice with a moiré lattice constant of $a_M \sim 5\text{nm}$. As shown in Fig. 1(a) the two sublattices of the hexagonal moiré lattice correspond to the MoTe₂ (*Mo*) and WSe₂ (*W*) layers, with the two sublattices connected by the interlayer hopping.

The combination of the strong spin-momentum locking of the monolayer materials and the AB stacking configuration reduces the magnitude of the interlayer tunnelling to a value much smaller than the intra-layer hopping of the WSe₂ moiré band [20]. The small interlayer coupling means that the two layers can be discussed separately and then the effects of the interlayer coupling considered. The atomic physics of the monolayer materials determines that the MoTe₂ layer has a narrower moiré conduction band than does the WSe₂ layer, so that the MoTe₂ layer may be regarded as strongly correlated with an upper and lower Hubbard band while the WSe₂ layer has a wider bandwidth and a carrier concentration

typically far from $n = 1$ and may be regarded as weakly correlated [12, 20]. The resulting density of states (DOS) is sketched in Fig. 1(b). The energy offset between the bands, defined here as Δ , and the total chemical potential μ can be controlled *in situ* by appropriate gate voltages.

Fig. 1(c) shows a qualitative phase diagram in the plane of band offset (Δ) and total density ($n = 1 + x$). At large positive Δ the MoTe₂ band is well separated from the bottom of the WSe₂ band. The first carriers added to the system go into the MoTe₂ layer, forming a correlated metal which at $n = 1$ becomes a triangular-lattice Mott insulator with 120° antiferromagnetic (AFM) order. At carrier concentration $n = 1$, decreasing Δ is predicted [12–16, 20] and observed [1] to cause a transition to a quantum anomalous Hall (QAH) state, followed by a transition to a conventional metallic state. At $\Delta > 0$, carriers in excess of the Mott concentration at half-filling ($n = 1$ per moiré unit cell) go into the WSe₂ band (if, as we assume, $U > \Delta$) and are coupled to the spins of the Mott insulator via an exchange coupling $J_K \sim t_h^2/\Delta$ derived perturbatively from the interlayer hybridization t_h , so that the MoTe₂/WSe₂ system can be described by an effective Kondo lattice model on the moiré scale whose study is the central topic of this paper.

Synthetic Kondo lattice models in moiré systems have been previously discussed in the context of the interplay between localized orbital and delocalized electrons in twisted bilayer [21] and trilayer graphene [22], and in relation to the orbital selective Mott transition in a two-band moiré TMD model [23]. More recently, a gate-tunable Kondo interaction in trilayer TMDs has been predicted to realize heavy fermion quantum criticality [24]. Here, we focus on how the combination of strong spin-orbit coupling and the non-local structure of the interlayer hybridization substantially enriches the physics relative to the standard Kondo-lattice/orbitally selective Mott transition picture.

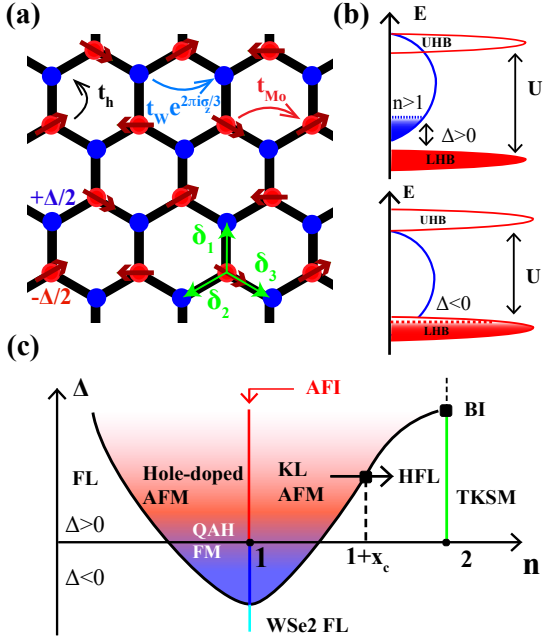


Figure 1. (a) Representation of real-space structure of MoTe₂/WSe₂ bilayer showing the two triangular sublattices of the honeycomb moiré lattice. Red and blue represent the centers of the Wannier functions describing the relevant states in the bottom (*Mo*) and top (*W*) layers, respectively. The nearest neighbor vector δ_i , the *Mo* – *W* energy difference Δ and the intralayer t_W/t_{Mo} and interlayer t_h hopping matrix elements are also indicated. (b) Schematic density of states for filling near $n = 1$ representing the *Mo* layer as a narrow-band strongly correlated system with lower (LHB) and upper (UHB) Hubbard bands separated by an energy gap U while the *W* layer is shown as a wide-band weakly correlated system. Upper panel: positive Δ ; showing filled *Mo* LHB and carriers added beyond $n = 1$ in the *W* layer. Lower panel: negative Δ ; mixed valent situation with potential for simultaneous occupancy of *Mo*- and *W*-layer states at $n = 1$. (c) Qualitative phase diagram of the AB stacked MoTe₂/WSe₂ bilayer as a function of hole carrier density n and displacement field Δ showing expected phases: at carrier density $n = 1$ as Δ is decreased the insulating 120° antiferromagnet (AFM) gives way to a QAH insulator and then to a Fermi liquid (FL). For $n > 1$ the system can be described by a Kondo lattice (KL) model. At other carrier concentrations different metallic phases occur including moderate mass (FL) and heavy mass (HFL) Fermi liquids; a hole-doped single band antiferromagnet (AFM) and a Kondo lattice antiferromagnet (KLAFM) with ordered magnetism on the *Mo* layer coupled to mobile carriers in the *W* layer. The HFL is connected to a topological Kondo semimetal (TKSM) at $n = 2$.

Derivation of the Kondo moiré lattice model.— The low-energy properties of the moiré system are described [12] by a Hubbard model on the honeycomb lattice shown in Fig. 1(a). The two sublattices of the honeycomb lattice give the centers of Wannier states formed from the *Mo* (red) and *W* (blue) sites respectively. Wannierization of band structure calculations [12] give same-sublattice hopping parameters $t_W \simeq 9\text{meV}$,

$t_{Mo} \simeq 4.5\text{meV}$ and an interlayer hopping $t_h \simeq 2\text{meV}$ shown as solid arrows in 1(a). The monolayer spin-orbit-coupling (SOC) implies that t_W has a spin-dependent complex phase factor $\pm 2\pi/3$ placing the *W* band minima at the Dirac points κ (spin up) and κ' (spin down) respectively; for details see Ref. [12, 20] or the SM [25]. The local interaction U which is taken to be the same on both layers for simplicity is believed to be large: $U/t_{Mo} \gg 1$ [11, 12] and for $\Delta > 0$ gives rise to filling $n = 1$ per moiré unit cell to a 120° AFM charge transfer insulator [12]. At nonzero electron doping $n = 1 + x$ ($x > 0$) the extra carriers go into the *W* charger-transfer band (blue shaded region of DOS in Fig. 1(b)) and *Mo* sites remain singly occupied. Due to the large bandwidth and the small doping x we assume that the correlation effects in the *W* band can be, at first approximation, ignored. The hybridization term t_h induces an effective spin-exchange Kondo coupling [25–27] between the dispersive electrons in the conduction band from the *W* and the local moments \mathbf{S}_r from the *Mo* layer. The resulting moiré Kondo-lattice (spin-fermion) model reads:

$$\begin{aligned} \bar{H} = & \sum_{\mathbf{k}\sigma} \xi_{\mathbf{k}\sigma} c_{\mathbf{k}\sigma}^\dagger c_{\mathbf{k}\sigma} \\ & + J_H \sum_{\langle \mathbf{r}, \mathbf{r}' \rangle_{Mo}} (S_{\mathbf{r}}^z S_{\mathbf{r}'}^z + \gamma S_{\mathbf{r}}^+ S_{\mathbf{r}'}^- + h.c.) \\ & + \frac{1}{2N} \sum_{\mathbf{r} \in Mo} \sum_{\mathbf{k}, \mathbf{p}} e^{-i(\mathbf{k}-\mathbf{p}) \cdot \mathbf{r}} J_{\mathbf{k}, \mathbf{p}} \mathbf{S}_{\mathbf{r}} \cdot c_{\mathbf{k}\sigma}^\dagger \sigma_{\sigma\sigma'} c_{\mathbf{p}\sigma'}, \end{aligned} \quad (1)$$

where $\xi_{\mathbf{k}\sigma} = -2t_W \sum_{j=1}^3 \cos(\mathbf{k} \cdot \mathbf{a}_j + 2\pi s_\sigma/3) - \epsilon_F$ is the electron dispersion for the *W* band, $\mathbf{a}_1 = \sqrt{3}a_M(1, 0)$, $\mathbf{a}_{2,3} = \sqrt{3}a_M(-1/2, \pm\sqrt{3}/2)$ are the lattice vectors with $a_M = 5\text{nm}$ is the moiré-lattice constant, $s_{\uparrow, \downarrow} = \pm 1$, and ϵ_F is the Fermi energy fixing the filling x of electrons in the conduction band $\sum_{\mathbf{r}, \sigma} \langle c_{\mathbf{r}\sigma}^\dagger c_{\mathbf{r}\sigma} \rangle / N = x$. The exchange J_H arises from a combination of the spin rotational invariant Heisenberg exchange in the *Mo* layer and virtual excitations in the *W* band mediated by t_h . The reduced spin rotational symmetry in the *W* layer induces the XXZ anisotropy $\gamma \neq 1/2$ and also Dzyaloshinskii–Moriya interactions [6]. For simplicity we use the Heisenberg form $\gamma = 1/2$ in Eq. (1) in our calculations and we treat J_H as a phenomenological parameter.

In the last term of Eq. (1), $J_{\mathbf{k}, \mathbf{p}} = J_K V_{\mathbf{k}}^* V_{\mathbf{p}}$ with $J_K = 2t_h^2 [1/\Delta + 1/(U - \Delta)]$ is the Kondo exchange and the hopping t_h between opposite sublattices gives the form factor $V_{\mathbf{k}} = \sum_{j=1}^3 e^{i\delta_j \cdot \mathbf{k}}$ with δ_j displayed as green arrows in Fig. 1(c). In proximity to the high-symmetry points κ and κ' , centers of the spin up and down Fermi sea at low-doping, respectively, the form factor takes the *p*-wave chiral form $V_{\kappa+\mathbf{k}} \simeq -3a_M(k_x - ik_y)/2$ and due to time-reversal symmetry $V_{\kappa'+\mathbf{k}} = V_{\kappa-\mathbf{k}}^*$. The displacement field dependence [24] and chirality will be seen to have important physics consequences.

To quantify the Kondo coupling at the Fermi energy we

introduce a Fermi surface (FS) averaged Kondo exchange \bar{J}_K as:

$$\bar{J}_K = \frac{J_K}{\rho_{\epsilon_F}} \frac{3\sqrt{3}a_M^2}{8\pi^2} \oint_{\text{FS}} dk_t \frac{|V_{\mathbf{k}}|^2}{|\nabla_{\mathbf{k}}\epsilon_{\mathbf{k}\sigma}|} \simeq \frac{xJ_K}{4\rho_{\epsilon_F}t_W}, \quad (2)$$

where the line integral is over the conduction electron FS, k_t is the component of \mathbf{k} along the tangent to the FS curve, ρ_{ϵ_F} is the DOS at the Fermi energy and in obtaining the explicit analytic form the W band dispersion was expanded to leading (quadratic) order around its minimum.

Mean-field theory.— In this section, we employ the mean-field theory of Abrikosov fermions [28–30] to study the competition between the magnetic and the HFL phase. For this purpose we factorize the local magnetic spin into charge neutral spinons $\mathbf{S}_{\mathbf{r}} = \chi_{\mathbf{r}\alpha}^\dagger \boldsymbol{\sigma}_{\alpha\beta} \chi_{\mathbf{r}\beta}/2$ subject to a constraint $\sum_{\sigma} \chi_{\mathbf{r}\sigma}^\dagger \chi_{\mathbf{r}\sigma} = 1$. In the following we adopt $\boldsymbol{\sigma}$ for the spin degrees of freedom. In our notation, $c_{\mathbf{r}}$ is a spin-doublet $(c_{\mathbf{r}\uparrow}, c_{\mathbf{r}\downarrow})^T$ and same for $\chi_{\mathbf{r}}$. We treat the Kondo interaction with an unrestricted Hartree Fock ansatz that is equally split across the hybridization order parameter Φ and magnetic order \mathbf{M} in the Mo layer, which can induce a non-zero polarization in the W layer \mathbf{m} . The HFL is captured by a non-vanishing amplitude of the hybridization $\Phi \equiv -\sum_{j=1}^3 \langle c_{\mathbf{r}+\delta_j}^\dagger \sigma_0 \chi_{\mathbf{r}} \rangle / 2$; the magnetic order is characterized by the variational parameters $\mathbf{M}_{\mathbf{r}} = (M^\parallel \cos \mathbf{Q} \cdot \mathbf{r}, M^\parallel \sin \mathbf{Q} \cdot \mathbf{r}, M^z)$ and $\mathbf{m}_{\mathbf{r}} = (m^\parallel \cos \mathbf{Q} \cdot \mathbf{r}, m^\parallel \sin \mathbf{Q} \cdot \mathbf{r}, m^z)$ with $\mathbf{Q} = \boldsymbol{\kappa} - \boldsymbol{\kappa}'$, $M^\parallel = \sum_{\mathbf{k}} [\langle \chi_{\mathbf{k}}^\dagger \sigma_+ \chi_{\mathbf{k}+\mathbf{Q}} \rangle + c.c.] / 2N$, $M^z = \sum_{\mathbf{k}} \langle \chi_{\mathbf{k}}^\dagger \sigma_z \chi_{\mathbf{k}} \rangle / 2N$, $m^\parallel = \sum_{\mathbf{k}} [V_{\mathbf{k}}^* \langle c_{\mathbf{k}}^\dagger \sigma_+ c_{\mathbf{k}+\mathbf{Q}} \rangle V_{\mathbf{k}+\mathbf{Q}} + c.c.] / 2N$ and $m^z = \sum_{\mathbf{k}} V_{\mathbf{k}}^* \langle c_{\mathbf{k}}^\dagger \sigma_z c_{\mathbf{k}} \rangle V_{\mathbf{k}} / 2N$. To obtain the values of the variational parameters we minimize the mean-field free-energy as detailed in the SM [25].

Fig. 2(a) shows the calculated mean-field phase diagram in the plane x versus J_H/t_W . The evolution of the mean-field parameters along the line cut, red line in Fig. 2(a), is displayed in Fig. 2(b). In the small doping regime $x < x_c$ the mean-field minimum describes a magnetic solution with in-plane 120° AFM (AFM-xy). The antiferromagnetic sign of J_K means that the conduction electron staggered magnetization m^\parallel is directed oppositely to \mathbf{M} shown as the orange line in Fig. 2(b). As doping x increases, $\rho_{\epsilon_F} \bar{J}_K$ grows as shown in the inset of Fig. 2(b), driving a transition of the general type discussed by Doniach [31] to a non-magnetic Kondo lattice state in which the system becomes paramagnetic $\mathbf{M} = 0$ and the localised moments hybridize with the conduction electrons giving rise to a large Fermi surface of heavy quasiparticles.

The transition between the AFM-xy phase and the HFL is first order: both the AFM-xy order parameter and the hybridization change discontinuously and the computed energies cross [Fig. 2(c)]. Across the phase transition the topology of the Fermi surface changes from electron like in the magnetic phase to hole like in the

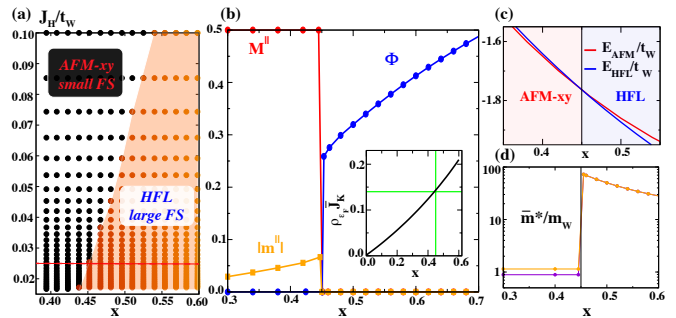


Figure 2. (a) Phase diagram in plane of WSe_2 filling x vs J_H/t_W calculated from solution of mean field equations. Blue does (white background) indicate regions of small Fermi surface metallic phase coexisting with 120° antiferromagnetic metallic order; red points (orange background) indicate regions of large Fermi surface heavy Fermi liquid phase. (b) Line cut at $J_H/t_W = 0.025$ showing x -dependence of the mean-field order parameters: hybridization Φ , local moment staggered magnetization M^\parallel and itinerant electron staggered magnetization $|m^\parallel|$. m^\parallel is opposite to M^\parallel ; we plot the absolute value of both quantities. The inset shows the effective Kondo exchange as a function of the doping x . A first order transition happens at the critical doping $x_c \simeq 0.45$ corresponding to $\rho_{\epsilon_F} \bar{J}_K \simeq 0.14$. (c) Energy of the two different phases as a function of x . (d) Evolution of the average quasiparticle mass as a function of x in logarithmic scale. The data are obtained setting $J_K/t_W = 1$ (bandwidth $9t_W$).

HFL phase. To gain insight on the nature of the transition, it is instructive to compare the low-doping behaviour $\rho_{\epsilon_F} \bar{J}_K \ll 1$ of the two energy scales in the Kondo lattice model: the Kondo temperature T_K and the magnetic energy E_{AFM} . Expanding to close to the bottom of the conduction band we have $T_K \simeq \epsilon_F \exp[-1/(\rho_{\epsilon_F} \bar{J}_K)]$ where for a quadratic dispersion the DOS is constant $\rho_{\epsilon_F} \simeq \rho_0 = 3\sqrt{3}a_M^2 m_W / (4\pi \hbar^2)$, $\epsilon_F \simeq x/(2\rho_0)$ and $m_W = \hbar^2/(9t_W a_M^2)$. On the other hand, in the magnetic state the Kondo coupling leads to a staggered polarization of conduction electrons which lowers the energy of the magnetic state: $E_{AFM} \simeq -3J_H M^2/2 - \bar{J}_K^2 \rho_{\epsilon_F} M^2/2$ ($M = 1/2$). The linear dependence of \bar{J}_K on doping x [Eq. (2)] implies that the scaling of the magnetic to paramagnetic transition is different from the standard Doniach scaling [31]. Finally, Fig. 2(c) shows the evolution of the average over the FS of the quasiparticle mass \bar{m}^* in logarithmic scale, where m^* is defined as $m^* = \hbar |\mathbf{k}_F| / |\mathbf{v}_F|$, $\bar{m}^* = \oint_{\text{FS}} dk_t m^* / (2\pi k_F)$ with \mathbf{v}_F and \mathbf{k}_F Fermi velocity and momentum, respectively. The transition is signalled by a drastic change of the quasiparticle mass. Interestingly, we find a diminution of \bar{m}^* increasing the doping x and a splitting of the quasiparticle mass in the magnetic regime.

Physical properties.— The HFL is characterized by the quasiparticle band structure in Fig. 3(a). In this regime the local moments in Mo layer participate to the total volume [32] enclosed by the FS and give rise to a large

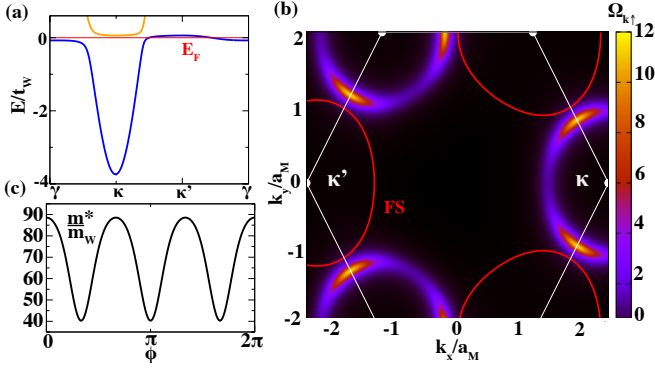


Figure 3. (a) Band structure of the heavy Fermi liquid along high-symmetry directions where the chiral Kondo coupling opens a topological hybridization gap between the upper (orange) and lower (blue) bands. The energy is measured with respect to the chemical potential. (b) Berry curvature of the lower heavy Fermi liquid band, where the red circles denote the hole Fermi surface. (c) Quasiparticle effective mass m^*/m_W as a function of the angle ϕ on the heavy electrons Fermi surface. The calculation has been performed at $x = 0.46$ and $J_K/t_W = 1$ (bandwidth $9t_W$).

hole-like FS which encircles the κ' (κ) point for \uparrow (\downarrow) electrons in the moiré Brillouin zone as shown by the solid red line in Fig. 3(b). We also show the variation of the quasiparticle mass around the Fermi surface in Fig. 3(c). In addition, we find quite unconventional properties that trace back to the form factor $V_{\mathbf{k}}$ in the Kondo coupling $J_{\mathbf{k},\mathbf{p}}$. The chiral nature of $V_{\mathbf{k}}$ gives rise to a chiral hybridization order parameter whose amplitude is proportional to $\langle c_{\kappa+\mathbf{k}\uparrow}^\dagger \chi_{\kappa+\mathbf{k}\uparrow} \rangle \propto \Phi(k_x - ik_y)$ for spin up and $\langle c_{\kappa'+\mathbf{k}\downarrow}^\dagger \chi_{\kappa'+\mathbf{k}\downarrow} \rangle \propto -\Phi(k_x + ik_y)$ for spin down and results into the topological character of the hybridization gap [33, 34]. The color code in Fig. 3(b) shows the Berry curvature $\Omega_{\mathbf{k}\uparrow} = -2 \text{Im} \langle \partial_{k_x} u_{\mathbf{k}\uparrow} | \partial_{k_y} u_{\mathbf{k}\uparrow} \rangle$ of the lower HFL band which is characterized by bright peaks at the position of the bare conduction electron FS. The opposite winding of spin \uparrow and \downarrow hybridization gap results in an opposite Berry curvature for the two spin $\Omega_{\mathbf{k}\uparrow} = -\Omega_{\mathbf{k}\downarrow}$. The HFL is adiabatically connected to a topological compensated Kondo semimetal at total filling $n = 2$ with a non-quantized quantum spin Hall effect [35].

In the opposite regime, at $x < x_c$ the ground state is characterized by a 120° AFM order with a small Fermi surface. The spin-flip scattering processes mediated by the modulation \mathbf{Q} connecting the spin \uparrow and \downarrow FSs give rise to a SOC term in the conduction electron Hamiltonian. As detailed in the SM [25] the expansion of the Hartree-Fock Hamiltonian close to the origin of the magnetic Brillouin zone gives:

$$\mathcal{H}_c(\mathbf{k}) = \left(\frac{\hbar^2 k^2}{2m_W} - \epsilon_F \right) \sigma_0 + \frac{9J_K a_M^2}{8} \sum_a d_a(\mathbf{k}) \sigma_a, \quad (3)$$

where $d_z(\mathbf{k}) = M^z(k_x^2 + k_y^2)$, $d_x(\mathbf{k}) = -M^\parallel(k_x^2 - k_y^2)$

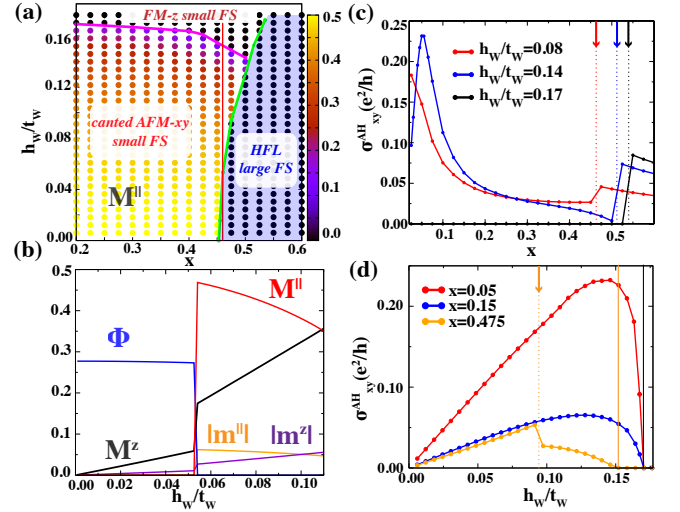


Figure 4. (a) Phase diagram plotted as a function of the W -layer carrier concentration x and the out-of-plane magnetic field h_W . The blue region denotes the HFL regime where the hybridization order parameter is finite. The color code before the green line shows the value of the in-plane antiferromagnetic order parameter M^\parallel . The solid green line shows the first order phase transition line. On the other hand, the magenta one shows the second order transition from the canted AFM-xy to the FM-z. (b) Evolution of the variational parameter along the line cut at $x = 0.46$ as a function of h_W/t_W . (c) Intrinsic contribution to the anomalous Hall conductivity for three different values of the Zeeman field. The vertical dashed lines denote the critical filling where the first order transition takes place. (d) Intrinsic AHE for different values of the filling x as a function of the Zeeman field. The vertical dashed line denotes the first order transition between the magnetic and the HFL phase, while the solid one the second order transition from a canted-AFM to the FM-z. Above this line the AHE vanishes. The calculation has been performed at $J_K/t_W = 1$, $J_H/t_W = 0.025$ (bandwidth $9t_W$).

and $d_y(\mathbf{k}) = 2M^\parallel k_x k_y$. The SOC splits the conduction electron FS giving rise to two different Fermi momenta k_F^\pm . A nonzero in-plane M^\parallel component in the Hamiltonian (3) induces a 2π -Berry phase winding around the origin of the magnetic Brillouin zone. In the presence of a nonzero Zeeman field we have a Berry curvature whose momentum space distribution depends on the value of the parameters in the Hamiltonian (3).

Finally, we study the evolution of the mean-field solution in an external magnetic field. Neglecting the orbital contribution we consider the effect of the Zeeman term $H_{\text{Zeeman}} = -h_{M_o} \sum_{\mathbf{r} \in M_o} S_{\mathbf{r}}^z - h_W \sum_{\mathbf{r} \in W} c_{\mathbf{r}}^\dagger \sigma_z c_{\mathbf{r}} / 2$ where $h_\alpha = g_\alpha \mu_B B$ and g_α is the gyromagnetic ratio for the two different TMDs ($g_{M_o} = 4$, $g_W = 6.1$ [36]). The phase diagram in the plane x vs B is shown in Fig. 4(a). At low-doping a small magnetic field introduces an out-of-plane magnetization M^z giving rise to a canted AFM-xy. Above the second order transition line (magenta line in Fig. 4(a)), that in the limit of vanishing doping takes the value $9(g_W/g_{M_o})J_H/2$, the canted AFM-xy turns into a

ferromagnetic solution along z (FM- z). For larger fillings, blue region in Fig. 4(a) starting at $x_c \simeq 0.45$ in the limit $h_W \rightarrow 0$, the small-field solution is the HFL. The line cut Fig. 4(b), red line at $x = 0.46$ in Fig. 4(a), shows the evolution of the variational parameters in magnetic field. In the HFL a small magnetic field induces a net magnetization M^z in the localized orbital χ . On the other hand, the Kondo hybridization is slightly affected by the external field. At a critical field displayed as a solid green line in Fig. 4(a) we find a first-order transition that is accompanied by an abrupt jump in the magnetization as well as by a discontinuous change in the conduction electron Fermi surface. The state above the first order line is a canted AFM-xy for $x < 0.5$ and a FM- z for $x > 0.5$.

Transport in magnetic field.— We use a Boltzmann equation approach to describe the transport of electrons in the different regimes of the phase diagram in Fig. 4(a), for details we refer to SM [25]. The Hall conductivity has contribution from an Ohmic part σ_{xy}^{Ohm} which depends on the extrinsic impurity scattering rate, and also has an intrinsic geometric contribution [37, 38] σ_{xy}^{AH} determined by the Berry curvature. In the HFL regime the non-vanishing hybridization implies that the neutral χ -spinon also contributes to the charge transport properties [39, 40]. Approximating the HFL FS shown in Fig. 3(b) with a circular FS with effective mass \bar{m}^* the Ohmic contribution takes the simple form $\sigma_{xx} = e^2\tau(1-x)/\bar{m}^*$ and $\sigma_{xy}^{\text{Ohm}} = -e^3B\tau^2(1-x)/\bar{m}^{*2}$. Conversely, in the magnetic regime only the concentration x of conduction electrons contributes to the charge transport properties. Assuming a single transport time, i.e. it is momentum- and band-independent, we find $\sigma_{xx} = e^2\tau x / (\sum_{\lambda} m_{\lambda}/2)$ and $\sigma_{xy}^{\text{Ohm}} = e^3\tau^2 Bx / (m_W \sum_{\lambda} m_{\lambda}/2)$ with $m_{\lambda} = m_W/[1 - \lambda J_K |M|/(4t_W)]$ ($\lambda = \pm$). As a result, increasing the magnetic field across the first order transition line [green line in Fig. 4(a)-(b)] we find a drastic jump in electrical conductivities, while in the HFL we have $1-x$ hole-like carriers in the AFM-xy phase a density of x electrons.

Moreover, the AFM-xy and the HFL are characterized by different intrinsic anomalous Hall conductivity σ_{xy}^{AH} . Figs. 4(c) shows the evolution of σ_{xy}^{AH} along different line cuts at constant Zeeman field as a function of doping x in the phase diagram Fig. 4(a). In the AFM regime, σ_{xy}^{AH} originates from the $d_x(\mathbf{k})$ and $d_y(\mathbf{k})$ terms in Eq. (3) induced by the in-plane component of the magnetic ordering. In the small doping regime we find a large AHE reaching a maximum $\sim 0.25e^2/h$ see Fig. 4(c). As we increase the doping the AHE decreases due to the smaller Berry curvature flux imbalance between the two Fermi surfaces with momenta $k_F^{\lambda} = \sqrt{2m_{\lambda}\epsilon_F}/\hbar^2$. Finally, above a critical density shown by the solid green line in the phase diagram Fig. 4(a) a first order transition from the canted AFM-xy to the HFL occurs. In the HFL regime, the anomalous Hall effect originates from the chiral hybridization gap with opposite sign for spin up and

down electrons which results in a non-quantized spin Hall effect. See SM [25] for details. A nonzero Zeeman field induces a flux imbalance between \uparrow and \downarrow which gives a finite AHE in the HFL as you can see in Fig. 4(c). In Fig. 4(d) we consider different concentration in the W -layer and we study the evolution as a function of the Zeeman field. We highlight that in the large field regime we enter in the FM- z regime where the AHE vanishes as displayed in the regions above the solid vertical lines in Fig. 4(c). We conclude observing that the non-quantized AHE depends on the parameters of the model (3) and can reach values $\sim e^2/h$ in the low-doping regime where a relatively small Zeeman field induces a large imbalance between the two Fermi surfaces.

Discussion.— We present a microscopic theory to explain the competition between AFM and the HFL in $\text{MoTe}_2/\text{WSe}_2$. As a result of the chiral nature of the Kondo exchange we find a first order transition as a function of the doping x that can also be driven by a magnetic field. We show how transport measurements can clearly distinguish the various phases. The AHE, which takes large values in the low-doping regime, can be further enhanced by spontaneous ferromagnetism induced by interaction between conduction electrons [41]. Extrinsic (scattering) mechanisms might also play a role in the observed AHE [42]. The paramagnetic HFL solution becomes at filling $n = 2$ a compensated topological Kondo semimetal with non-quantized quantum spin Hall effect. Finally, we notice that the effect of quantum fluctuations beyond the mean-field approach as well as the role of anisotropic effects in the exchange between magnetic moments are important questions for future research.

Acknowledgements.— We thank Kin Fai Mak and Jie Shan for sharing with us experimental data prior to its publication and for insightful discussions. We have benefited from discussions with Elio König, Piers Coleman, John Sous, Raquel Queiroz, Corentin Bertrand and Roberto Raimondi. This work was partially supported by the Air Force Office of Scientific Research under Grant No. FA9550-20-1-0260 (J.C.) and Grant No. FA9550-20-1-0136 (J.H.P.) and the Alfred P. Sloan Foundation through a Sloan Research Fellowship (J.H.P.). J.H.P. acknowledges the Aspen Center for Physics, where some of this work was completed, which is supported by National Science Foundation grant PHY-1607611. J.Z. acknowledges support from the NSF MRSEC program through the Center for Precision-Assembled Quantum Materials (PAQM) - DMR-2011738. Flatiron Institute is a division of the Simons Foundation.

[1] T. Li, S. Jiang, B. Shen, Y. Zhang, L. Li, Z. Tao, T. Devakul, K. Watanabe, T. Taniguchi, L. Fu, J. Shan, and K. F. Mak, Quantum anomalous hall effect from inter-

- twined moiré bands, *Nature* **600**, 641 (2021).
- [2] T. Li, S. Jiang, L. Li, Y. Zhang, K. Kang, J. Zhu, K. Watanabe, T. Taniguchi, D. Chowdhury, L. Fu, J. Shan, and K. F. Mak, Continuous mott transition in semiconductor moiré superlattices, *Nature* **597**, 350 (2021).
- [3] A. Ghiotto, E.-M. Shih, G. S. S. G. Pereira, D. A. Rhodes, B. Kim, J. Zang, A. J. Millis, K. Watanabe, T. Taniguchi, J. C. Hone, L. Wang, C. R. Dean, and A. N. Pasupathy, Quantum criticality in twisted transition metal dichalcogenides, *Nature* **597**, 345 (2021).
- [4] H. Li, S. Li, E. C. Regan, D. Wang, W. Zhao, S. Kahn, K. Yumigeta, M. Blei, T. Taniguchi, K. Watanabe, S. Tongay, A. Zettl, M. F. Crommie, and F. Wang, Imaging two-dimensional generalized wigner crystals, *Nature* **597**, 650 (2021).
- [5] F. Wu, T. Lovorn, E. Tutuc, and A. H. MacDonald, Hubbard model physics in transition metal dichalcogenide moiré bands, *Phys. Rev. Lett.* **121**, 026402 (2018).
- [6] T. Devakul, V. Crépel, Y. Zhang, and L. Fu, Magic in twisted transition metal dichalcogenide bilayers, *Nature Communications* **12**, 10.1038/s41467-021-27042-9 (2021).
- [7] J. Zang, J. Wang, J. Cano, and A. J. Millis, Hartree-fock study of the moiré hubbard model for twisted bilayer transition metal dichalcogenides, *Phys. Rev. B* **104**, 075150 (2021).
- [8] J. Zang, J. Wang, J. Cano, A. Georges, and A. J. Millis, Dynamical mean-field theory of moiré bilayer transition metal dichalcogenides: Phase diagram, resistivity, and quantum criticality, *Phys. Rev. X* **12**, 021064 (2022).
- [9] J. Wang, J. Zang, J. Cano, and A. J. Millis, Staggered Pseudo Magnetic Field in Twisted Transition Metal Dichalcogenides: Physical Origin and Experimental Consequences, arXiv e-prints, arXiv:2110.14570 (2021), arXiv:2110.14570 [cond-mat.mes-hall].
- [10] A. Wietek, J. Wang, J. Zang, J. Cano, A. Georges, and A. Millis, Tunable Stripe Order and Weak Superconductivity in the Moiré Hubbard Model, arXiv e-prints, arXiv:2204.04229 (2022), arXiv:2204.04229 [cond-mat.str-el].
- [11] H. Pan, M. Xie, F. Wu, and S. D. Sarma, Topological phases in ab-stacked $\text{mote}_2/\text{wse}_2$: \mathbb{Z}_2 topological insulators, chern insulators, and topological charge density waves (2021).
- [12] T. Devakul and L. Fu, Quantum anomalous hall effect from inverted charge transfer gap (2021).
- [13] Y.-M. Xie, C.-P. Zhang, J.-X. Hu, K. F. Mak, and K. T. Law, Valley-polarized quantum anomalous hall state in moiré $\text{mote}_2/\text{wse}_2$ heterobilayers, *Phys. Rev. Lett.* **128**, 026402 (2022).
- [14] Y.-M. Xie, C.-P. Zhang, and K. T. Law, Topological $p_x + ip_y$ inter-valley coherent state in moiré $\text{mote}_2/\text{wse}_2$ heterobilayers (2022).
- [15] M. Xie, H. Pan, F. Wu, and S. D. Sarma, Nematic excitonic insulator in transition metal dichalcogenide moiré heterobilayers (2022).
- [16] Z. Dong and Y.-H. Zhang, Excitonic chern insulator and kinetic ferromagnetism in $\text{mote}_2/\text{wse}_2$ moiré bilayer (2022).
- [17] M. Davydova, Y. Zhang, and L. Fu, Itinerant spin polaron and metallic ferromagnetism in semiconductor moiré superlattices (2022).
- [18] G.-B. Liu, W.-Y. Shan, Y. Yao, W. Yao, and D. Xiao, Three-band tight-binding model for monolayers of group-vib transition metal dichalcogenides, *Phys. Rev. B* **88**, 085433 (2013).
- [19] A. Kormányos, G. Burkard, M. Gmitra, J. Fabian, V. Zólyomi, N. D. Drummond, and V. Fal'ko, $k \cdot p$ theory for two-dimensional transition metal dichalcogenide semiconductors, *2D Materials* **2**, 022001 (2015).
- [20] Y. Zhang, T. Devakul, and L. Fu, Spin-textured chern bands in AB-stacked transition metal dichalcogenide bilayers, Proceedings of the National Academy of Sciences **118**, 10.1073/pnas.2112673118 (2021).
- [21] Z.-D. Song and B. A. Bernevig, Matbg as topological heavy fermion: I. exact mapping and correlated insulators (2021).
- [22] A. Ramires and J. L. Lado, Emulating heavy fermions in twisted trilayer graphene, *Phys. Rev. Lett.* **127**, 026401 (2021).
- [23] A. Dalal and J. Ruhman, Orbitally selective mott phase in electron-doped twisted transition metal-dichalcogenides: A possible realization of the kondo lattice model, *Phys. Rev. Research* **3**, 043173 (2021).
- [24] A. Kumar, N. C. Hu, A. H. MacDonald, and A. C. Potter, Gate-tunable heavy fermion quantum criticality in a moiré kondo lattice (2021).
- [25] See Supplementary Material at url ... for details on the continuum and the tight binding Hamiltonian, the Schrieffer-Wolff transformation, the mean-field theory of Abrikosov fermions.
- [26] J. R. Schrieffer and P. A. Wolff, Relation between the anderson and kondo hamiltonians, *Phys. Rev.* **149**, 491 (1966).
- [27] A. H. MacDonald, S. M. Girvin, and D. Yoshioka, $\frac{t}{U}$ expansion for the hubbard model, *Phys. Rev. B* **37**, 9753 (1988).
- [28] P. Coleman and N. Andrei, Kondo-stabilised spin liquids and heavy fermion superconductivity, *Journal of Physics: Condensed Matter* **1**, 4057 (1989).
- [29] T. Senthil, M. Vojta, and S. Sachdev, Weak magnetism and non-fermi liquids near heavy-fermion critical points, *Physical Review B* **69**, 10.1103/physrevb.69.035111 (2004).
- [30] J. Pixley, R. Yu, and Q. Si, Quantum phases of the shastry-sutherland kondo lattice: Implications for the global phase diagram of heavy-fermion metals, *Physical Review Letters* **113**, 10.1103/physrevlett.113.176402 (2014).
- [31] S. Doniach, The Kondo lattice and weak antiferromagnetism, *Physica B+C* **91**, 231 (1977).
- [32] M. Oshikawa, Topological approach to luttinger's theorem and the fermi surface of a kondo lattice, *Phys. Rev. Lett.* **84**, 3370 (2000).
- [33] M. Dzero, K. Sun, V. Galitski, and P. Coleman, Topological kondo insulators, *Phys. Rev. Lett.* **104**, 106408 (2010).
- [34] M. Dzero, J. Xia, V. Galitski, and P. Coleman, Topological kondo insulators, *Annual Review of Condensed Matter Physics* **7**, 249 (2016).
- [35] C. L. Kane and E. J. Mele, Quantum spin hall effect in graphene, *Physical Review Letters* **95**, 10.1103/physrevlett.95.226801 (2005).
- [36] C. Robert, H. Dery, L. Ren, D. Van Tuan, E. Courtade, M. Yang, B. Urbaszek, D. Lagarde, K. Watanabe, T. Taniguchi, T. Amand, and X. Marie, Measurement of conduction and valence bands g -factors in a transition

- metal dichalcogenide monolayer, *Phys. Rev. Lett.* **126**, 067403 (2021).
- [37] N. P. Ong, Geometric interpretation of the weak-field hall conductivity in two-dimensional metals with arbitrary fermi surface, *Phys. Rev. B* **43**, 193 (1991).
- [38] F. D. M. Haldane, Berry curvature on the fermi surface: Anomalous hall effect as a topological fermi-liquid property, *Physical Review Letters* **93**, 10.1103/physrevlett.93.206602 (2004).
- [39] D. Chowdhury, I. Sodemann, and T. Senthil, Mixed-valence insulators with neutral fermi surfaces, *Nature Communications* **9**, 10.1038/s41467-018-04163-2 (2018).
- [40] L. B. Ioffe and A. I. Larkin, Gapless fermions and gauge fields in dielectrics, *Phys. Rev. B* **39**, 8988 (1989).
- [41] K. Sun, H. Yao, E. Fradkin, and S. A. Kivelson, Topological insulators and nematic phases from spontaneous symmetry breaking in 2d fermi systems with a quadratic band crossing, *Phys. Rev. Lett.* **103**, 046811 (2009).
- [42] N. Nagaosa, J. Sinova, S. Onoda, A. H. MacDonald, and N. P. Ong, Anomalous hall effect, *Rev. Mod. Phys.* **82**, 1539 (2010).

Chiral Kondo Effect in AB Stacked MoTe₂/WSe₂ bilayers

Daniele Guerci,¹ Jie Wang,¹ Jiawei Zang,² Jennifer Cano,^{3,1} J. H. Pixley,^{4,1} and Andrew Millis^{1,2}

¹Center for Computational Quantum Physics, Flatiron Institute, New York, New York 10010, USA

²Department of Physics, Columbia University, 538 Wst 120th Street, New York, NY 10027

³Department of Physics and Astronomy, Stony Brook University, Stony Brook, New York 11974, USA

⁴Department of Physics and Astronomy, Center for Materials Theory, Rutgers University, Piscataway, New Jersey 08854, USA

These supplementary materials contain the details of analytic calculations as well as additional numerical details supporting the results presented in the main text.

I. THE KONDO LATTICE HAMILTONIAN

In this section we detail the connection between the tight-binding model and the Schrieffer-Wolff transformation to obtain the Kondo lattice Hamiltonian given in the main text.

A. The tight-binding Hamiltonian

Assuming W -layer weakly correlated the tight-binding Hamiltonian that describes the low-energy properties of the system reads $H = H_0 + H_W + H_t$:

$$\begin{aligned} H_0 &= -\frac{\Delta}{2}(N_{Mo} - N_W) + U \sum_{\mathbf{r} \in Mo} n_{\mathbf{r}\uparrow} n_{\mathbf{r}\downarrow} \\ H_W &= -t_W \sum_{\langle \mathbf{r}, \mathbf{r}' \rangle \in W} e^{-i\nu_{\mathbf{r}, \mathbf{r}'} 2\pi s_\sigma / 3} c_{\mathbf{r}\sigma}^\dagger c_{\mathbf{r}'\sigma}, \\ H_t &= -t_{Mo} \sum_{\langle \mathbf{r}, \mathbf{r}' \rangle \in Mo} c_{\mathbf{r}\sigma}^\dagger c_{\mathbf{r}'\sigma} - t_h \sum_{\langle \mathbf{r}, \mathbf{r}' \rangle} c_{\mathbf{r}}^\dagger c_{\mathbf{r}'}. \end{aligned} \quad (1)$$

We notice that differently from H_0 and H_W the contribution H_t changes the local configuration in the Mo layer.

B. The Schrieffer-Wolff transformation

We assume that U is the largest energy scale, $U \gg t_{Mo}$, and $\Gamma(\epsilon_F)/\Delta < 1$ where $\Gamma(\epsilon_F)$ is the hybridization function:

$$\Gamma(\epsilon_F) = \pi t_h^2 \rho(\epsilon_F) \langle V_{\mathbf{k}}^* V_{\mathbf{k}} \rangle_{FS} = \pi t_h^2 \left(\frac{3\sqrt{3}a_M^2}{8\pi^2} \right) \oint_{FS} dk_t \frac{V_{\mathbf{k}}^* V_{\mathbf{k}}}{|\nabla_{\mathbf{k}} \epsilon_{\mathbf{k}\sigma}|}. \quad (2)$$

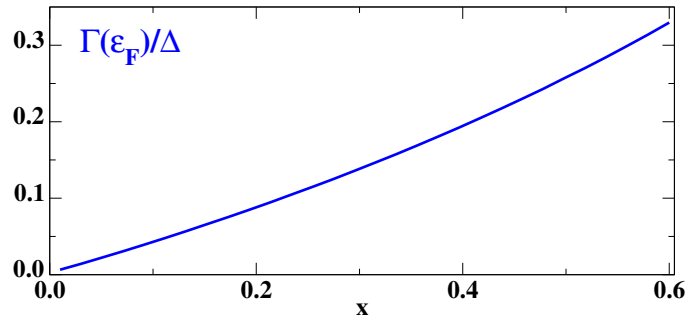


Figure 1. Evolution of $\Gamma(\epsilon_F)/\Delta$ as a function of the filling x of the conduction band.

Fig. 1 show the evolution of $\Gamma(\epsilon_F)$ as a function of the filling x for the value of t_h^2/Δ corresponding to $J_K/t_W = 1$ value used for the numerical calculations shown in the manuscript. Within these assumptions valence fluctuations in Mo layer are suppressed. We now observe that the tunneling H_t can be decomposed as:

$$H_t = \sum_{q=-1}^1 \sum_{d=-1}^1 T_{q,d}, \quad (3)$$

where $T_{q,d}$ gathers all tunneling events that change the number of electrons unbalance between Mo and W by q and the double occupancies in Mo layer by d . We list the $T_{q,d}$ operators below:

$$\begin{aligned} T_{+1,+1} &= -t_h \sum_{\mathbf{r} \in Mo} \sum_{\sigma} \sum_{j=1}^3 n_{\mathbf{r}\bar{\sigma}} f_{\mathbf{r}\sigma}^\dagger c_{\mathbf{r}+\delta_j\sigma}, \\ T_{+1,0} &= -t_h \sum_{\mathbf{r} \in Mo} \sum_{\sigma} \sum_{j=1}^3 h_{\mathbf{r}\bar{\sigma}} f_{\mathbf{r}\sigma}^\dagger c_{\mathbf{r}+\delta_j\sigma}, \\ T_{0,+1} &= -t_{Mo} \sum_{\mathbf{r} \in Mo} \sum_{\sigma} \sum_{j=1}^3 \left[n_{\mathbf{r}\bar{\sigma}} f_{\mathbf{r}\sigma}^\dagger f_{\mathbf{r}+\gamma_j\sigma} h_{\mathbf{r}+\gamma_j\bar{\sigma}} + h_{\mathbf{r}+\gamma_j\bar{\sigma}} f_{\mathbf{r}+\gamma_j\sigma}^\dagger f_{\mathbf{r}\sigma} n_{\mathbf{r}\bar{\sigma}} \right], \\ T_{0,0} &= -t_{Mo} \sum_{\mathbf{r} \in Mo} \sum_{\sigma} \sum_{j=1}^3 \left[n_{\mathbf{r}\bar{\sigma}} f_{\mathbf{r}\sigma}^\dagger f_{\mathbf{r}+\gamma_j\sigma} n_{\mathbf{r}+\gamma_j\bar{\sigma}} + h_{\mathbf{r}\bar{\sigma}} f_{\mathbf{r}\sigma}^\dagger f_{\mathbf{r}+\gamma_j\sigma} h_{\mathbf{r}+\gamma_j\bar{\sigma}} + h.c. \right], \end{aligned} \quad (4)$$

where we have introduced the operator $f_{\mathbf{r}\sigma}$ for electrons in Mo -layer, $T_{-q,-d} = T_{q,d}^\dagger$, $n_{\mathbf{r}\sigma} = f_{\mathbf{r}\sigma}^\dagger f_{\mathbf{r}\sigma}$ and $h_{\mathbf{r}\sigma} = 1 - n_{\mathbf{r}\sigma}$. Before moving on, we notice that the intralayer hopping H_{Mo} does not change the charge imbalance $N_{Mo} - N_W$ ($q = 0$), i.e. H_{Mo} commutes with $N_{Mo} - N_W$ ($[N_{Mo} - N_W, H_{Mo}] = 0$). Moreover, $[N_{Mo} - N_W, T_{q,d}] = 2qT_{q,d}$ and

$$\sum_{\mathbf{r} \in Mo} [n_{\mathbf{r}\uparrow} n_{\mathbf{r}\downarrow}, T_{q,d}] = dT_{q,d}. \quad (5)$$

We seek an unitary transformation $U = \exp(-iS)$ which eliminates hops between states with different numbers of doubly occupied sites and interlayer charge imbalance [1, 2]:

$$\bar{H} \equiv e^{iS} H e^{-iS} = H + [iS, H] + \frac{[iS, [iS, H]]}{2!} + \dots, \quad (6)$$

where we applied the Baker-Campbell-Hausdorff formula. We now notice that to the lowest order in the expansion we have:

$$[H_0, iS] = \sum_{q,d}^{(q,d) \neq 0} T_{q,d}, \quad (7)$$

where in previous sum we exclude the term with $q = 0$ and $d = 0$ in shorthand notation $(q, d) \neq 0$. We readily realize that the solution of Eq. (7) reads:

$$S = -i \sum_{q,d}^{(q,d) \neq 0} \frac{T_{q,d}}{dU - q\Delta}. \quad (8)$$

From the latter expression we find:

$$\bar{H} = H_0 + T_{0,0} + H_W + \frac{1}{2} \sum_{q,d}^{(q,d) \neq 0} \sum_{q',d'}^{(q',d') \neq 0} \frac{[T_{q,d}, T_{q',d'}]}{-q\Delta + dU} + \sum_{q,d}^{(q,d) \neq 0} \frac{[T_{q,d}, H_W + T_{0,0}]}{-q\Delta + dU} + O([H_W + T_{0,0}]S^2). \quad (9)$$

Projecting the model in the low-energy subspace with one-electron in Mo layer, i.e. $n_{\mathbf{r}} = 1$ for $\mathbf{r} \in Mo$, we find that the latter term vanishes. Furthermore, the projection constraints $q' = -q$ and $d' = -d$:

$$\bar{H} = -t_W \sum_{(\mathbf{r}, \mathbf{r}') \in W} e^{-i\nu_{\mathbf{r}, \mathbf{r}'} 2\pi s_\sigma / 3} c_{\mathbf{r}\sigma}^\dagger c_{\mathbf{r}'\sigma} - \mu N_W + \frac{1}{2} \sum_{q,d}^{(q,d) \neq 0} \frac{[T_{q,d}, T_{-q,-d}]}{dU - q\Delta}, \quad (10)$$

where the constant energy term $\Delta N_W/2$ has been absorbed in the chemical potential shift and $T_{0,0}$ vanishes in the low-energy subspace. By performing straightforward calculations we find that the commutator in Eq. (10) gives:

$$\begin{aligned} \frac{1}{2} \sum_{q,d}^{(q,d) \neq 0} \frac{[T_{q,d}, T_{-q,-d}]}{dU - q\Delta} = & t_h^2 \left(\frac{1}{\Delta} + \frac{1}{U - \Delta} \right) \sum_{\mathbf{r} \in M_o} \sum_{j,l=1}^3 \mathbf{S}_{\mathbf{r}} \cdot c_{\mathbf{r}+\delta_j, \sigma}^\dagger \sigma_{\sigma\sigma'} c_{\mathbf{r}+\delta_l, \sigma'} + \frac{4t_{Mo}^2}{U} \sum_{\langle \mathbf{r}, \mathbf{r}' \rangle \in A} \mathbf{S}_{\mathbf{r}} \cdot \mathbf{S}_{\mathbf{r}'} \\ & + t_h^2 \left(\frac{1}{\Delta} - \frac{1}{U - \Delta} \right) \sum_{\mathbf{k}} |V_{\mathbf{k}}|^2 c_{\mathbf{k}}^\dagger c_{\mathbf{k}}. \end{aligned} \quad (11)$$

Expanding close to the bottom of the conduction band [$\kappa(\kappa')$ for \uparrow (\downarrow)] $|V_{\kappa/\kappa'+\mathbf{k}}|^2 \simeq 9(a_M k)^2/4$ we realize that the latter terms can be simply accounted by a redefinition of the bare mass $m_W \rightarrow m_W/[1 + (t_h/\Delta - t_h/(U - \Delta))t_h/(2t_W)]$. Finally, we find the effective spin-fermion Hamiltonian:

$$\bar{H} = \sum_{\mathbf{k}} \xi_{\mathbf{k}\sigma} c_{\mathbf{k}\sigma}^\dagger c_{\mathbf{k}\sigma} + J_H \sum_{\langle \mathbf{r}, \mathbf{r}' \rangle \in A} \mathbf{S}_{\mathbf{r}} \cdot \mathbf{S}_{\mathbf{r}'} + \frac{1}{2N} \sum_{\mathbf{r} \in M_o} \sum_{\mathbf{k}, \mathbf{p}} e^{-i(\mathbf{k}-\mathbf{p}) \cdot \mathbf{r}} J_{\mathbf{k}, \mathbf{p}} \mathbf{S}_{\mathbf{r}} \cdot c_{\mathbf{k}\sigma}^\dagger \sigma_{\sigma\sigma'} c_{\mathbf{p}\sigma'}, \quad (12)$$

where $J_H = 4t_{Mo}^2/U$, $J_{\mathbf{k}, \mathbf{p}} = J_K V_{\mathbf{k}}^* V_{\mathbf{p}}$, $J_K = 2t_h^2[1/\Delta + 1/(U - \Delta)]$, $\xi_{\mathbf{k}\sigma} = \epsilon_{\mathbf{k}\sigma} - \epsilon_F$, $\epsilon_{\mathbf{k}\sigma}$ is the electron dispersion and ϵ_F fixes the number of electron in the conduction band. The dispersion relation reads $\epsilon_{\mathbf{k}\sigma} = -2t_W \sum_{j=1}^3 \cos(\mathbf{k} \cdot \mathbf{a}_j + 2\pi s_\sigma/3)$, $\mathbf{a}_1 = \sqrt{3}a_M(1, 0)$, $\mathbf{a}_{2,3} = \sqrt{3}a_M(-1/2, \pm\sqrt{3}/2)$ are the lattice vectors with $a_M = 5\text{nm}$ the moiré cell lattice constant. The form factor is $V_{\mathbf{k}} = \sum_{j=1}^3 e^{i\mathbf{k} \cdot \delta_j}$. Despite U is large and J_H small the particular form of the exchange interaction $J_{\mathbf{k}, \mathbf{p}} = J_K V_{\mathbf{k}}^* V_{\mathbf{p}}$ gives rise to a non-trivial competition between a low-density magnetic phase and a paramagnetic heavy Fermi liquid.

1. On the higher-order corrections

Higher order corrections in the expansion lower the symmetry of the spin interaction in the Mo -layer. This can be simply realized noticing that the phase factor in the Hamiltonian H_W lower the spin-symmetry of the model to $U(1)$ around z . Including higher-order hopping processes mediated by t_h gives an XXZ spin model with Dzyaloshinskii–Moriya interactions:

$$H_S = J_H \sum_{\langle \mathbf{r}, \mathbf{r}' \rangle \in M_o} (S_{\mathbf{r}}^z S_{\mathbf{r}'}^z + \gamma S_{\mathbf{r}}^+ S_{\mathbf{r}'}^- + h.c.) + D \sum_{\langle \mathbf{r}, \mathbf{r}' \rangle \in M_o} (\mathbf{S}_{\mathbf{r}} \times \mathbf{S}_{\mathbf{r}'})_z, \quad (13)$$

we refer to Ref. [3] for additional details. For simplicity we consider the isotropic limit $\gamma = 1/2$ and $D = 0$ in our calculations.

II. THE MEAN-FIELD APPROACH

In this section we detail the mean-field of Abrikosov fermions discussed in the main text. We perform the decomposition of the spin-1/2 into spinons $\mathbf{S}_{\mathbf{r}} = \chi_{\mathbf{r}\alpha}^\dagger \sigma_{\alpha\beta} \chi_{\mathbf{r}\beta}/2$ and performing the mean-field decomposition in the magnetic and excitonic channels we obtain the mean-field Hamiltonian:

$$\begin{aligned} \bar{H}_{\text{mf}} = & \lambda \sum_{\mathbf{k}} \chi_{\mathbf{k}}^\dagger \chi_{\mathbf{k}} + \frac{h^z}{2} \sum_{\mathbf{k}} \chi_{\mathbf{k}}^\dagger \sigma^z \chi_{\mathbf{k}} + \frac{h^\parallel}{2} \sum_{\mathbf{k}} [\chi_{\mathbf{k}+\mathbf{Q}}^\dagger \sigma^- \chi_{\mathbf{k}} + h.c.] + \sum_{\mathbf{k}\sigma} \xi_{\mathbf{k}\sigma} c_{\mathbf{k}\sigma}^\dagger c_{\mathbf{k}\sigma} \\ & + \frac{M^z}{2} \sum_{\mathbf{k}} J_{\mathbf{k}, \mathbf{k}} c_{\mathbf{k}}^\dagger \sigma^z c_{\mathbf{k}} + \frac{M^\parallel}{2} \sum_{\mathbf{k}} [J_{\mathbf{k}+\mathbf{Q}, \mathbf{k}} c_{\mathbf{k}+\mathbf{Q}}^\dagger \sigma^- c_{\mathbf{k}} + h.c.] \\ & + J_K \sum_{\mathbf{k}} [V_{\mathbf{k}}^* \Phi^* c_{\mathbf{k}}^\dagger \chi_{\mathbf{k}} + h.c.]. \end{aligned} \quad (14)$$

The mean-field free-energy reads:

$$\begin{aligned} F_{\text{mf}} = & -k_B T \sum_{\mathbf{k}} \sum_{\lambda} \log [1 + e^{-E_{\mathbf{k}\lambda}/k_B T}] + 2J_K N |\Phi|^2 + \frac{3J_H N}{2} M^{\parallel 2} \\ & - 3J_H N M^z - J_K M^z N m^z - J_K N M^\parallel m^\parallel - \lambda N + N \mu x, \end{aligned} \quad (15)$$

where $E_{\mathbf{k}\lambda}$ is the mean-field dispersion relation. The mean-field solution is obtained by minimizing F_{mf} with respect to the variational parameters $M^z, M^\parallel, \Phi, m^z, m^\parallel$. The Lagrange multiplier λ imposes the Gutzwiller constraint $\sum_{\mathbf{k}} \langle \chi_{\mathbf{k}}^\dagger \chi_{\mathbf{k}} \rangle / N = 1$, while the chemical potential μ fixes the number of particle in conduction band $\sum_{\mathbf{k}} \langle c_{\mathbf{k}}^\dagger c_{\mathbf{k}} \rangle / N = x$. Taking the saddle point of Eq. (15) with respect to the variational parameters gives a set of self-consistency equations that are solved by find-root algorithm.

A. Energetics of the HFL and AFM states

In this section we detail the weak coupling expansion to determines the characteristic energy scales of the AFM and HFL phases that are the RKKY energy and the Kondo temperature, respectively. We will also introduce the effective model describing the quasiparticle excitations in the two different regimes.

1. AFM

In the magnetic regime the local moments $\mathbf{S}_{\mathbf{r}}$ form a 120° AFM order with $\langle \mathbf{S}_{\mathbf{r}} \rangle = (M^\parallel \cos \mathbf{Q} \cdot \mathbf{r}, M^\parallel \sin \mathbf{Q} \cdot \mathbf{r}, M^z)$, $\mathbf{Q} = \kappa - \kappa'$, correspondingly the conduction electron Hamiltonian reads:

$$\bar{H}_{\text{mf}}^c = \sum_{\mathbf{k}} \xi_{\mathbf{k}\sigma} c_{\mathbf{k}\sigma}^\dagger c_{\mathbf{k}\sigma} + \frac{J_K M^z}{2} \sum_{\mathbf{k}} |V_{\mathbf{k}}|^2 c_{\mathbf{k}}^\dagger \sigma^z c_{\mathbf{k}} + \frac{J_K M^\parallel}{2} \sum_{\mathbf{k}} \left[V_{\mathbf{k}}^* V_{\mathbf{k}+\mathbf{Q}} c_{\mathbf{k}}^\dagger \sigma^+ c_{\mathbf{k}+\mathbf{Q}} + h.c. \right]. \quad (16)$$

In the limit of low-doping the Fermi surface is a small electron pocket around $\kappa(\uparrow)$ and $\kappa'(\downarrow)$ that are folded into the origin of the magnetic Brillouin zone γ_m , depicted in Fig. 4(b). Expanding close to quadratic order around γ_m and keeping only the two lowest energy bands we find the continuum model:

$$\bar{H}_{\text{mf}}^c = \sum_{\mathbf{k}} c_{\mathbf{k}}^\dagger \left[\left(\frac{\hbar^2 k^2}{2m_W} - \epsilon_F \right) \sigma_0 + \frac{9J_K a_M^2}{8} \sum_a d_a(\mathbf{k}) \sigma_a \right] c_{\mathbf{k}}, \quad (17)$$

where $d_z(\mathbf{k}) = M^z k^2$, $d_x(\mathbf{k}) = -M^\parallel (k_x^2 - k_y^2)$ and $d_y(\mathbf{k}) = 2M^\parallel k_x k_y$. We readily realize that due to the SOC term the spin is no longer a good quantum number, the eigenstates $|u_{\mathbf{k}\lambda}\rangle$ are labeled by $\lambda = \pm$ and the corresponding eigenvalues are $\epsilon_{\mathbf{k}\lambda} = (\hbar^2 k^2 / 2m_W - \epsilon_F) + \lambda 9J_K a_M^2 k^2 |M| / 8$ with $|M| = \sqrt{(M^z)^2 + (M^\parallel)^2}$. We observe that the theory is O(3) invariant under rotation of the magnetization $M^a \rightarrow R_{ab} M^b$. The resulting stabilization energy does not depend on the orientation of the local moments. The Fermi momentum obtained by setting $\epsilon_{\mathbf{k}\lambda} = 0$ reads $k_F^\pm = \sqrt{2m_\lambda \epsilon_F / \hbar^2}$ where $m_\lambda = m_W / [1 + \lambda (J_K / 8t_W)]$ and the Fermi energy is $\epsilon_F \simeq x / (\sum_\lambda \rho_\lambda)$ with $\rho_\lambda = \rho_0 m_\lambda / m_W$. We notice that in the Kondo regime J_K is smaller than the bandwidth of conduction electrons $9t_W$ so that the mass is always positive. The kinetic energy variation with respect to the normal state reads:

$$\delta \epsilon_{\text{mf}}^c = \epsilon_{\text{mf}}^c - \epsilon_{J_K=0}^c = -\rho_0 \bar{J}_K^2 |M|^2 / 2, \quad (18)$$

where \bar{J}_K is the average over the FS of the Kondo exchange. We conclude that the total energy per site in the magnetic regime is given by:

$$\epsilon_{\text{mf}} = -3J_H |M|^2 / 2 - \rho_0 \bar{J}_K^2 |M|^2 / 2. \quad (19)$$

The energy gain from the coupling between the conduction band and the local moments goes quadratically in the electron density x .

We conclude observing that in the large J_K regime corresponding to a very small charge transfer energy one of the two band in Eq. (17) develops a negative curvature around $k = 0$. Including higher-order corrections in momentum regularize the theory in the UV allowing for a finite doping in conduction band. It is known [4] that in this regime the model is unstable towards ferromagnetism which opens a gap at the quadratic band touching. The analysis requires including interaction effects in the conduction electrons and goes beyond the regime of validity of the Kondo lattice model we investigate here.

2. HFL

In the paramagnetic regime electrons are described by the mean-field Hamiltonian reads:

$$\bar{H}_{\text{mf}} = \sum_{\mathbf{k}\sigma} \xi_{\mathbf{k}\sigma} c_{\mathbf{k}\sigma}^\dagger c_{\mathbf{k}\sigma} + \lambda \sum_{\mathbf{k}} \chi_{\mathbf{k}}^\dagger \chi_{\mathbf{k}} + J_K \sum_{\mathbf{k}\sigma} \left[V_{\mathbf{k}}^* \Phi^* c_{\mathbf{k}}^\dagger \chi_{\mathbf{k}} + h.c. \right]. \quad (20)$$

We easily realize that the Green's function of the problem reads:

$$\mathbf{G}_\sigma^{-1}(\mathbf{k}, i\epsilon) = \begin{pmatrix} i\epsilon - \lambda & -J_K \Phi^* V_{\mathbf{k}}^* \\ -J_K \Phi V_{\mathbf{k}} & i\epsilon - \xi_{\mathbf{k}\sigma} \end{pmatrix}, \quad (21)$$

so that the saddle-point equation for the bosonic amplitude Φ can be written as:

$$\Phi = -\frac{T}{2N} \sum_{\mathbf{k}\sigma} \sum_{i\epsilon} V_{\mathbf{k}}^* \mathcal{G}_{\chi,\sigma}(\mathbf{k}, i\epsilon) J_K V_{\mathbf{k}} \Phi G_{c,\sigma}(\mathbf{k}, i\epsilon), \quad (22)$$

where $\mathcal{G}_{\chi,\sigma}(\mathbf{k}, i\epsilon) = (i\epsilon - \lambda)^{-1}$ is the bare Green's function and $G_{c,\sigma}(\mathbf{k}, i\epsilon) = [i\epsilon - \xi_{\mathbf{k}\sigma} - \Sigma_{c,\sigma}(\mathbf{k}, i\epsilon)]^{-1}$ with

$$\Sigma_{c,\sigma}(\mathbf{k}, i\epsilon) = J_K^2 |\Phi|^2 |V_{\mathbf{k}}|^2 / (i\epsilon - \lambda). \quad (23)$$

Discarding the $\Phi = 0$ solution the equation reduces to

$$\frac{1}{J_K} = \frac{1}{2N} \sum_{\mathbf{k}\sigma} \frac{f(E_{\mathbf{k}-\sigma}) - f(E_{\mathbf{k}+\sigma})}{\sqrt{(\xi_{\mathbf{k}\sigma} - \lambda)^2 + 4J_K^2 |\Phi|^2 |V_{\mathbf{k}}|^2}} = \frac{1}{2N} \sum_{\mathbf{k}\sigma} \frac{\theta(-E_{\mathbf{k}-\sigma})}{\sqrt{(\xi_{\mathbf{k}\sigma} - \lambda)^2 + 4J_K^2 |\Phi|^2 |V_{\mathbf{k}}|^2}}, \quad (24)$$

where $E_{\mathbf{k}\pm} = (\xi_{\mathbf{k}\sigma} + \lambda)/2 \pm \sqrt{(\xi_{\mathbf{k}\sigma} - \lambda)^2 + 4J_K^2 |\Phi|^2 |V_{\mathbf{k}}|^2}/2$ and the RHS is obtained taking the we took the zero temperature limit and considering the case $x < 1$ where only the lower band is filled. In addition we also have the self-consistent equation for λ :

$$\frac{T}{N} \sum_{\mathbf{k}\sigma} \sum_{i\epsilon} \frac{1}{i\epsilon - \lambda - \Sigma_{\chi,\sigma}(\mathbf{k}, i\epsilon)} = 1 \implies \frac{1}{2N} \sum_{\mathbf{k}\sigma} \theta(-E_{\mathbf{k}-\sigma}) \left(1 + \frac{\xi_{\mathbf{k}\sigma} - \lambda}{\sqrt{(\xi_{\mathbf{k}\sigma} - \lambda)^2 + 4J_K^2 |\Phi|^2 |V_{\mathbf{k}}|^2}} \right) = 1. \quad (25)$$

The onset of the HFL instability can be determined by determining the instability condition of the normal state to hybridization. In this case the solution of Eq. (25) is $\lambda = 0$, i.e. the local moments are pinned at the Fermi level, and Eq. (22) becomes:

$$\frac{1}{J_K} + \Pi_{\chi c}^0(\mathbf{q} \rightarrow 0, i\Omega = 0) = 0, \quad (26)$$

where $\Pi_{\chi c}^0(\mathbf{q} \rightarrow 0, \tau) = -\langle T_\tau (\hat{V}_{\mathbf{q}=0}(\tau) \hat{V}_{\mathbf{q}=0}^\dagger) \rangle / N$, $\hat{V}_{\mathbf{q}=0} = \sum_{\mathbf{k}} V_{\mathbf{k}}^* c_{\mathbf{k}}^\dagger \chi_{\mathbf{k}} / \sqrt{2}$ and $\Pi_{\chi c}^0(\mathbf{q} \rightarrow 0, i\Omega) = \int_0^\beta e^{i\Omega\tau} \Pi_{\chi c}^0(\mathbf{q} \rightarrow 0, \tau)$. Expanding close to the bottom of the band Eq. (26) becomes:

$$\frac{1}{J_K} - \frac{\rho_0}{2} \int_{\epsilon_F}^{E_\Lambda} \frac{|V_\epsilon|^2}{\epsilon - \epsilon_F} - \frac{\rho_0}{2} \int_0^{\epsilon_F} \frac{|V_\epsilon|^2}{\epsilon_F - \epsilon} = 0, \quad (27)$$

where $|V_\epsilon| = 9a_M^2 k_\epsilon^2 / 4$ with $k_\epsilon = \sqrt{2m_W \epsilon / \hbar^2}$. The integral is characterized by a log singularity at ϵ_F . We introduce the IR cutoff T_K , $\epsilon \rightarrow \epsilon \pm T_K$, that regularize the divergence. Finally, by performing simple calculations we find:

$$T_K \simeq \epsilon_F e^{-1/(\rho_0 J_K)}. \quad (28)$$

Since the average over the Fermi surface \bar{J}_K goes linearly with the doping x in conduction band we find that the Kondo temperature is exponentially suppressed in the limit $x \rightarrow 0^+$.

III. TRANSPORT PROPERTIES

In this section we detail the evaluation of the transverse and longitudinal conductivities in the various phases of the phase diagram.

A. Charge transport in the HFL

In the paramagnetic regime the local moments fractionalize giving rise to a finite density of holes in MoTe₂ layer. In this regime the field $\Phi_{\mathbf{r}}$ is equivalent to the holon operator carrying physical charge -1 [5], i.e. opposite to the electron charge. As a result both conduction electrons c and spinon χ contribute to the charge current. Within the

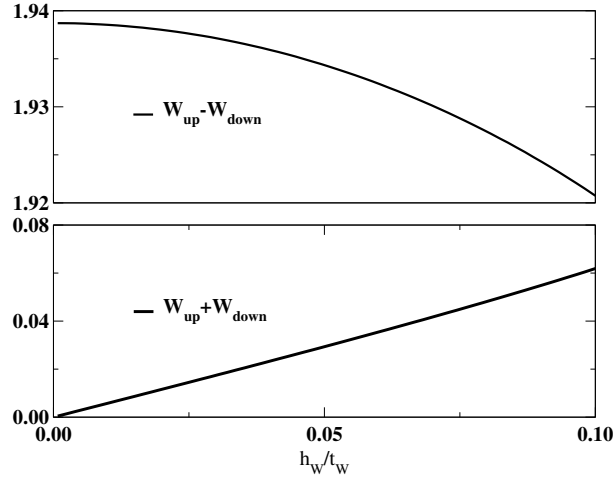


Figure 2. Spin Hall effect (top panel) and anomalous Hall effect (bottom panel) in the HFL as a function of the Zeeman field.

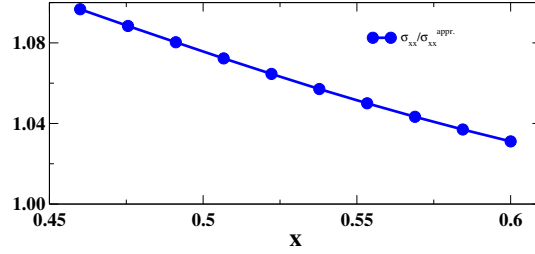


Figure 3. Ratio between the numerical evaluation of Eq. (29) and $\sigma_{xx} = e^2 \tau (1 - x) / \bar{m}^*$ obtained assuming a circular Fermi surface with average velocity.

semiclassical Boltzmann equation approach and in the relaxation time approximation the transport properties are simply obtained as integrals over the quasiparticle Fermi surface [6, 7]:

$$\sigma_{xx} = \frac{3\sqrt{3}a_M^2 e^2 \tau}{8\pi^2} \sum_{\sigma} \oint_{FS} dk_t \frac{\bar{v}_{F,\sigma}^x \bar{v}_{F,\sigma}^x}{\hbar |\bar{\mathbf{v}}_{F,\sigma}|}, \quad (29)$$

and

$$\sigma_{xy} \equiv \sigma_{xy}^{\text{Ohm}} + \sigma_{xy}^{\text{AH}} = \frac{3\sqrt{3}a_M^2 e^3 \tau^2 B}{8\pi^2 \hbar} \sum_{\sigma} \oint_{FS} dk_t \frac{\bar{v}_{F,\sigma}^y [\bar{v}_{F,\sigma}^y \partial_{k_x} - \bar{v}_{F,\sigma}^x \partial_{k_y}]}{\hbar |\bar{\mathbf{v}}_{F,\sigma}|} \bar{v}_{F,\sigma}^x + \frac{e^2}{2\pi\hbar} \sum_{\sigma} \oint_{FS} dk_t \mathbf{t} \cdot \mathbf{A}_{\sigma}(\mathbf{k}), \quad (30)$$

where the anomalous Hall contribution σ_{xy}^{AH} arises from the circulation of the Berry connection $\mathbf{A}_{\sigma}(\mathbf{k}) = i \langle u_{\mathbf{k}\sigma} | \partial_{k_a} u_{\mathbf{k}\sigma} \rangle$, with $|u_{\mathbf{k}\sigma}\rangle$ occupied eigenstate of the Hamiltonian in Eq. (20), along the FS. In Eqs. (29) and (30) k_t is the component of \mathbf{k} along the tangent \mathbf{t} to the FS curve. We notice that the FS of the heavy quasiparticle is obtained by the set of \mathbf{k} points solution of the equation:

$$\text{heavy FS} : \xi_{\mathbf{k}\sigma} - J_K^2 |\Phi|^2 |V_{\mathbf{k}}|^2 / \lambda = 0, \quad (31)$$

where the second term comes from the conduction electron self-energy $\Sigma_{c,\sigma}(\mathbf{k}, 0)$ introduced in Eq. (23) computed at $i\omega = 0$. The Fermi velocity $\mathbf{v}_{F,\sigma}$ is obtained replacing $\mathbf{k} \rightarrow \mathbf{k} + e\mathbf{A}(t)/\hbar$ in $\xi_{\mathbf{k}\sigma} = Z_{\mathbf{k}\sigma} [\xi_{\mathbf{k}\sigma} - J_K^2 |\Phi|^2 |V_{\mathbf{k}}|^2 / \lambda]$ and expanding to linear order around the FS we find $\xi_{\mathbf{k}_F + \frac{e}{\hbar} \mathbf{A}(t)\sigma} \simeq e \bar{\mathbf{v}}_F \cdot \mathbf{A}(t)$ where:

$$\bar{\mathbf{v}}_{F,\sigma} = \frac{Z_{\mathbf{k}_F,\sigma}}{\hbar} \nabla_{\mathbf{k}} [\xi_{\mathbf{k}\sigma} - J_K^2 |\Phi|^2 |V_{\mathbf{k}}|^2 / \lambda] \Big|_{\mathbf{k}_F}, \quad (32)$$

and $Z_{\mathbf{k},\sigma} = [1 - \partial_z \Sigma_{c,\sigma}(\mathbf{k}, z)|_{z=0}]^{-1}$ is the quasiparticle weight. The evaluation of σ_{xx} and σ_{xy}^{Ohm} is considerably simplified observing that the Fermi surface consists of a hole-pocket around $\boldsymbol{\kappa}'$ for spin \uparrow and $\boldsymbol{\kappa}$ for spin \downarrow , respectively.

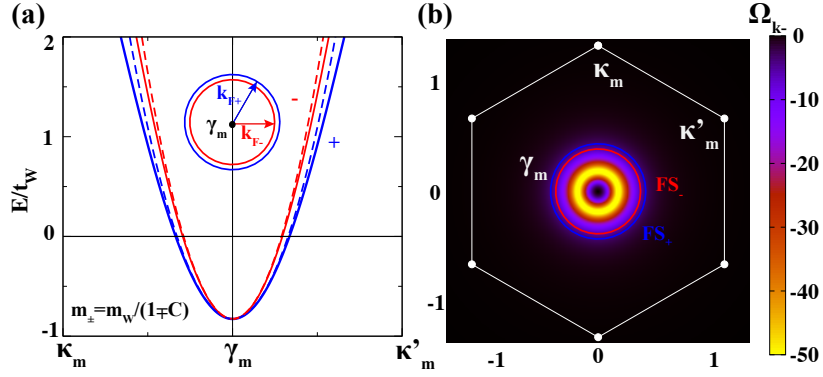


Figure 4. (a) Dispersion of the electrons close to the bottom of the conduction band. Dashed lines are obtained with the continuum Hamiltonian (??) while the solid ones are the lowest energy bands of the mean-field Hamiltonian (??). (b) Berry curvature around the origin of the magnetic Brillouin zone. Solid lines show the two Fermi surfaces. The calculations has been performed at doping $x = 0.08$, $J_K/t_W = 1$, $J_H/t_W = 0.025$ and magnetic field $h_W/t_W = 0.08$.

Assuming a circular hole-like Fermi surface with average mass \bar{m}^* the longitudinal contribution becomes

$$\sigma_{xx} = 2 \frac{e^2 \tau}{\bar{m}^*} \left(\frac{\sqrt{3} a_M^2}{8\pi^2} \right) k_F^2 \int_0^{2\pi} d\phi \cos^2 \phi = \frac{e^2 \tau}{\bar{m}^*} \left(2\pi k_F^2 \frac{\sqrt{3} a_M^2}{8\pi^2} \right) = \frac{e^2 \tau (1-x)}{\bar{m}^*}. \quad (33)$$

As a sanity check we show in Fig. 3 the ratio between Eq. (33) and the numerical evaluation of Eq. (29) for various concentrations of electrons in the W -layer. By following the same line of reasoning we obtain $\sigma_{xy}^{\text{Ohm}} = -e^3 \tau^2 B (1-x)/\bar{m}^{*2}$. We now look at the anomalous contribution σ_{xy}^{AH} which can be conveniently written as $\sigma_{xy}^{\text{AH}} = e^2 (W_\uparrow + W_\downarrow)/h$ where $W_\sigma = \int d^2 \mathbf{k} f(\epsilon_{\mathbf{k}\sigma}) \Omega_\sigma(\mathbf{k}) / (2\pi)$ and $\Omega_\sigma(\mathbf{k}) = \partial_{k_x} A_\sigma^y(\mathbf{k}) - \partial_{k_y} A_\sigma^x(\mathbf{k})$. Due to the opposite winding of spin \uparrow and \downarrow we find that in the absence of a magnetic field $W_\uparrow = -W_\downarrow$. We observe that the difference $W_\uparrow - W_\downarrow$ gives a finite spin Hall (SH) conductivity [8] even in the absence of the external field. Fig. 2 shows $W_\uparrow \pm W_\downarrow$ as a function of the magnetic field at doping $x = 0.46$ and $J_K/t_W = 1$. The small value of $W_\uparrow + W_\downarrow$ at finite B follows from the Berry curvature distribution which is peaked around the bare FS of the conduction electrons. As a result we find a small AH contribution and a large SH one.

1. The magnetic regime

We now turn our attention in the magnetic regime where only the c -electrons contribute to charge transport. The low-energy Hamiltonian is given in Eq. (17) and describes electrons with dispersion relation $\epsilon_{\mathbf{k}\lambda} = \hbar^2 k^2 / 2m_\lambda$ shown in Fig. 4(a) and group velocity $\mathbf{v}_{\mathbf{k}\lambda} = \hbar \mathbf{k} / m_\lambda$ with $m_\lambda = m_W / [1 - \lambda J_K |M| / (4t_W)]$ and $\lambda = \pm$. Under the assumption of a single transport time, i.e. momentum- and band-independent, we apply Eqs. (29) and (30) to find $\sigma_{xx} = e^2 \tau x / (\sum_\lambda m_\lambda / 2)$ and $\sigma_{xy}^{\text{Ohm}} = e^3 \tau^2 B x / (m_W \sum_\lambda m_\lambda / 2)$. We now conclude our analysis considering the AHE contribution coming from the the Berry phase winding introduced by the $d_x(\mathbf{k})$ and $d_y(\mathbf{k})$ terms in Eq. (17). In the absence of an external magnetic field $M^z = 0$ and the eigenstates are simply $|u_{\mathbf{k}\pm}\rangle = (1, \pm e^{-2i\varphi_{\mathbf{k}}}) \sqrt{2}$ with 2π -Berry phase around the origin of the magnetic Brillouin zone. A small Zeeman term opens a gap in the band structure and gives rise to a finite Berry curvature $\Omega_\pm(\mathbf{k})$:

$$\Omega_\pm(\mathbf{k}) = \pm \frac{64h^2 k^2 \eta^2}{\left[16k^4 \eta^2 + \left(2h + \frac{m_\uparrow - m_\downarrow}{m_\uparrow m_\downarrow} k^2 \right)^2 \right]^{3/2}}, \quad (34)$$

where $\eta = 9J_K M^\parallel / 8$ and $m_{\uparrow/\downarrow} = m_W / [1 \pm J_K M^z / (4t_W)]$. We notice that the Berry curvature is an even function of k , vanishes quadratically at $k = 0$ and takes its maximum value at finite momentum k . The maximum is located at $k_{\text{max}}^4 = h^2 / (8\eta^2)$ for $M^z = 0$. The momentum space distribution in the magnetic moiré Brillouin zone is given in Fig. 4(b). We observe that from Eq. (34) the anomalous Hall conductivity is obtained as:

$$\sigma_{xy}^{\text{AH}} = \frac{e^2}{2\pi h} \sum_\lambda \int d^2 \mathbf{k} \Omega_\lambda(\mathbf{k}) f(\epsilon_{\mathbf{k}\lambda} - \mu), \quad (35)$$

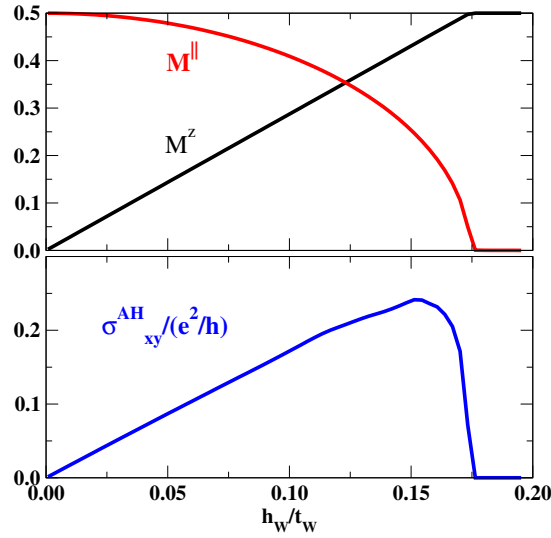


Figure 5. Top panel: evolution of the in-plane and out-of-plane magnetization as a function of the applied field. Bottom panel: anomalous Hall conductivity. The calculations has been performed at doping $x = 0.08$, $J_K/t_W = 1$, $J_H/t_W = 0.025$.

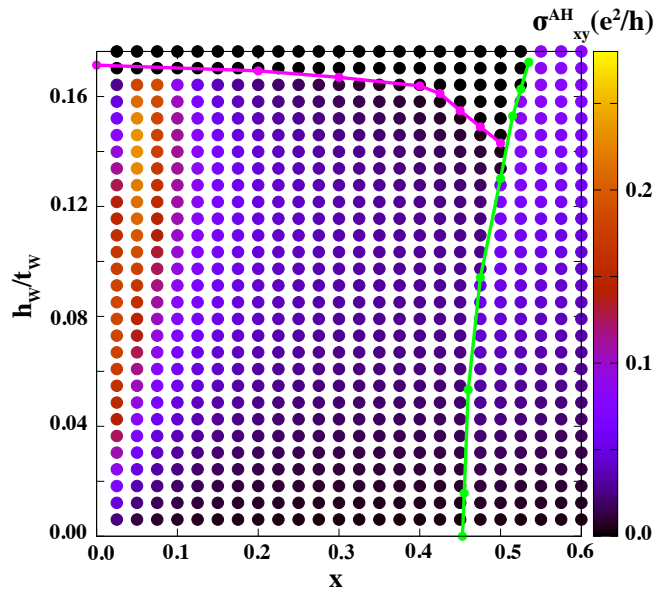


Figure 6. Intrinsic contribution to AHE conductivity in the plane of W -layer concentration x and h_W Zeeman field.

which in the zero temperature limit becomes:

$$\sigma_{xy}^{\text{AH}} = \frac{e^2}{h} \int_{k_F^-}^{k_F^+} dk k \Omega_+(k) = \frac{e^2}{h} \frac{h[k^2(m_\downarrow - m_\uparrow) - 2hm_\uparrow m_\downarrow]}{\sqrt{16k^4\eta^2(m_\uparrow m_\downarrow)^2 + [k^2(m_\uparrow - m_\downarrow) + 2hm_\uparrow m_\downarrow]^2}} \Bigg|_{k_F^-}^{k_F^+}. \quad (36)$$

Fig. 5 shows the evolution of the anomalous Hall conductivity in the low-density regime. Finally, Fig. 6 gives bird's-eye view over the anomalous Hall effect in the plane of the W -layer concentration and the Zeeman field.

-
- [1] J. R. Schrieffer and P. A. Wolff, Phys. Rev. **149**, 491 (1966), URL <https://link.aps.org/doi/10.1103/PhysRev.149.491>.
 - [2] A. H. MacDonald, S. M. Girvin, and D. Yoshioka, Phys. Rev. B **37**, 9753 (1988), URL <https://link.aps.org/doi/10.1103/PhysRevB.37.9753>.
 - [3] T. Devakul, V. Crépel, Y. Zhang, and L. Fu, Nature Communications **12** (2021), URL <https://doi.org/10.1038/2Fs41467-021-27042-9>.
 - [4] K. Sun, H. Yao, E. Fradkin, and S. A. Kivelson, Phys. Rev. Lett. **103**, 046811 (2009), URL <https://link.aps.org/doi/10.1103/PhysRevLett.103.046811>.
 - [5] D. Chowdhury, I. Sodemann, and T. Senthil, Nature Communications **9** (2018), URL <https://doi.org/10.1038/2Fs41467-018-04163-2>.
 - [6] N. P. Ong, Phys. Rev. B **43**, 193 (1991), URL <https://link.aps.org/doi/10.1103/PhysRevB.43.193>.
 - [7] F. D. M. Haldane, Physical Review Letters **93** (2004), URL <https://doi.org/10.1103/2Fphysrevlett.93.206602>.
 - [8] C. L. Kane and E. J. Mele, Physical Review Letters **95** (2005), URL <https://doi.org/10.1103/2Fphysrevlett.95.226801>.